STRUCTURAL BIOLOGY COMMUNICATIONS

ISSN 2053-230X

Structures of additional crystal forms of Satellite tobacco mosaic virus grown from a variety of salts

Alexander McPherson*

Department of Molecular Biology and Biochemistry, University of California, 530A Steinhaus Hall, Irvine, CA 92697-3900, USA. *Correspondence e-mail: amcphers@uci.edu

Received 11 June 2021
Accepted 2 November 2021

Edited by K. K. Kim, Sungkyunkwan University School of Medicine, Republic of Korea

Keywords: Satellite tobacco mosaic virus; STMV; ion channels; crystallization; symmetry; decapsidation; anions.

PDB references: Satellite tobacco mosaic virus, 5bkl; 5bkn; 5bkq; 7m2t; 7m2v; 7m3r; 7m3t; 7m50; 7m54; 7m57

Supporting information: this article has supporting information at journals.iucr.org/f

The structures of new crystal forms of Satellite tobacco mosaic virus (STMV) are described. These belong to space groups $I2$, $P2_12_12$ (a low-resolution form), $R3$ ($H3$) and $P23$. The $R3$ crystals are 50%/50% twinned, as are two instances of the $P23$ crystals. The $I2$ and $P2_12_12$ crystals were grown from ammonium sulfate solutions, as was one crystal in space group $P23$, while the $R3$ and the other $P23$ crystals were grown from sodium chloride, sodium bromide and sodium nitrate. The monoclinic and orthorhombic crystals have half a virus particle as the asymmetric unit, while the rhombohedral and cubic crystals have one third of a virus particle. RNA segments organized about the icosahedral twofold axes were present in crystals grown from ammonium sulfate and sodium chloride, as in the canonical $I222$ crystals (PDB entry 4oq8), but were not observed in crystals grown from sodium bromide and sodium nitrate. Bromide and nitrate ions generally replaced the RNA phosphates present in the $I222$ crystals, including the phosphates seen on fivefold axes, and were also found at threefold vertices in both the rhombohedral and cubic forms. An additional anion was also found on the fivefold axis 5 Å from the first anion, and slightly outside the capsid in crystals grown from sodium chloride, sodium bromide and sodium nitrate, suggesting that the path along the symmetry axis might be an ion channel. The electron densities for RNA strands at individual icosahedral dyads, as well as at the amino-terminal peptides of protein subunits, exhibited a diversity of orientations, in particular the residues at the ends.

1. Introduction

Satellite tobacco mosaic virus (STMV), the properties of which are summarized in Table 1, is a spherical satellite virus to the helical, rod-shaped Tobacco mosaic virus (TMV) (Valverde & Dodds, 1986 1987; Valverde *et al.*, 1991; Ban & McPherson, 1995). It is the second smallest virus currently known (Ban & McPherson, 1995) and is a $T = 1$ icosahedron (Caspar & Klug, 1962) composed of 60 identical protein subunits of 159 amino acids, each of which has a molecular mass of 14 700 Da (Valverde & Dodds, 1986, 1987; Valverde *et al.*, 1991). The capsid proteins exhibit a canonical eight-stranded Swiss-roll β-barrel structure with a long (37-residue) extended amino-terminal tail that is responsible (Larson *et al.*, 1993, 1998) in a great part for protein dimer formation and for interaction with the genomic, positive-sense ssRNA molecule of 1058 nucleotides (Mirkov *et al.*, 1989), the 3′ end of which can be histidinylated (Felden, 1994). The entire virus particle has a molecular mass of about 1.5 MDa, about a quarter of which is RNA (Mirkov *et al.*, 1989; Ban *et al.*, 1995). The structure of STMV, crystals of which are shown in Fig. 1, was initially solved by isomorphous replacement and phase extension (Larson *et al.*, 1993, 1998).

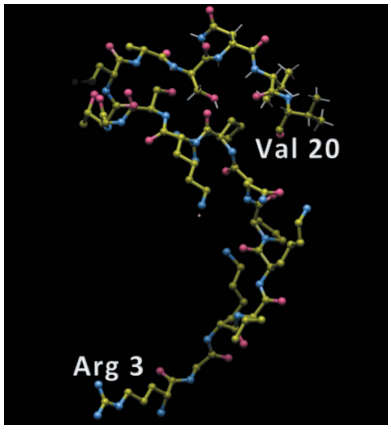

Table 1
Satellite tobacco mosaic virus particle properties.

Symmetry	T = 1 icosahedral (exact 532)
No. of protein subunits	60
RNA genome	1058 nucleotides (30 segments observable)
Symmetry axes	12 fivefolds, 20 threefolds, 30 twofolds
Protein subunit molecular mass (Da)/No. of atoms	17542/1155
RNA molecular mass (Da)/ No. of atoms	339379/26160
Particle molecular mass (Da)/ No. of atoms	1393039/95520
Particle diameter (Å)	164
Source	TMV/STMV coinfected tobacco leaves
Master virus	Tobacco mosaic virus (TMV)
Previous PDB depositions	1a34, 4nia, 4oq8, 4oq9

A noteworthy feature of these analyses was the appearance in the electron-density map of double-stranded helical segments of RNA at the 30 icosahedral twofold axes of the virus, which would ostensibly constitute nearly 45% of the entire genome. Using, in part, unusually large crystals grown in microgravity aboard the US Space Shuttle (Day & McPherson, 1992), the virus particle, both protein and visible RNA, was refined using *X-PLOR* (Brünger *et al.*, 1987, 1998) to a resolution of 1.8 Å (Larson *et al.*, 1998). Data were recorded from 17 different crystals at room temperature using a conventional rotating-anode source and a multiwire area detector (San Diego Multiwire Systems, San Diego, California, USA).

We subsequently devised conditions for the cryo-preservation of large STMV crystals and collected X-ray diffraction intensities to 1.42 Å resolution from a single flash-cooled crystal (Fig. 1*a*). We re-refined the model in an *I*222 unit cell, with a quarter of the virus particle as the asymmetric unit, against the original room-temperature data, with a resolution cutoff of 1.8 Å, and also refined the model against the full 1.42 Å resolution cryogenic crystal data, with the latter consisting of 613 720 independent reflections (Larson *et al.*, 2014). Both the room-temperature and the flash-cooled structures have been deposited in the PDB (PDB entries 4nia, 1a34, 4oq8 and 4oq9) and are henceforth referred to as the canonical virus models.

STMV is noteworthy for several reasons, largely due to its ease of crystallization, the large size of its crystals and the appearance of a large portion of its nucleic acid in electron-density maps. It played a major role in microgravity crystallization experiments aboard the US Space Shuttle, the Russian Space Station MIR and the International Space Station (DeLucas *et al.*, 1992; Day & McPherson, 1992; Koszelak *et al.*, 1996; McPherson, 1992, 1996, 1997), it provided a sample for the application of ultrasound to virus crystals (Stephanidis *et al.*, 2007) and was instrumental in light-scattering studies of macromolecular crystal nucleation and growth (Malkin *et al.*, 1993; Malkin & McPherson, 1993) and the study of macromolecular crystal growth by atomic force microscopy (Land *et al.*, 1996; McPherson, 2013; Kuznetsov *et al.*, 2010). It was the first virus crystal structure to undergo a molecular-dynamics simulation (Freddolino *et al.*, 2006). Its pronounced RNA component has been of particular interest from the standpoint of viral RNA structure (Day *et al.*, 2001; Archer *et al.*, 2013; Zeng *et al.*, 2012; McPherson, 2013) and icosahedral virus assembly (Larson & McPherson, 2001; McPherson, 2005, 2013).

We noted many years ago that when STMV was crystallized (Table 2) under our standard conditions (Koszelak *et al.*, 1989; 16–20% ammonium sulfate buffered at pH 6.5 at 298 K) but at 277 K (4°C), a different crystal habit appeared (Fig. 1*b*). The crystals at 277 K were apex-truncated triangular plates, often with a thickness of up to about 0.25 mm. When transferred to room temperature the crystals were stable for about a week, but subsequently dissolved and recrystallized to give the usual *I*222 form (Fig. 1*a*). X-ray analysis showed the new crystals to

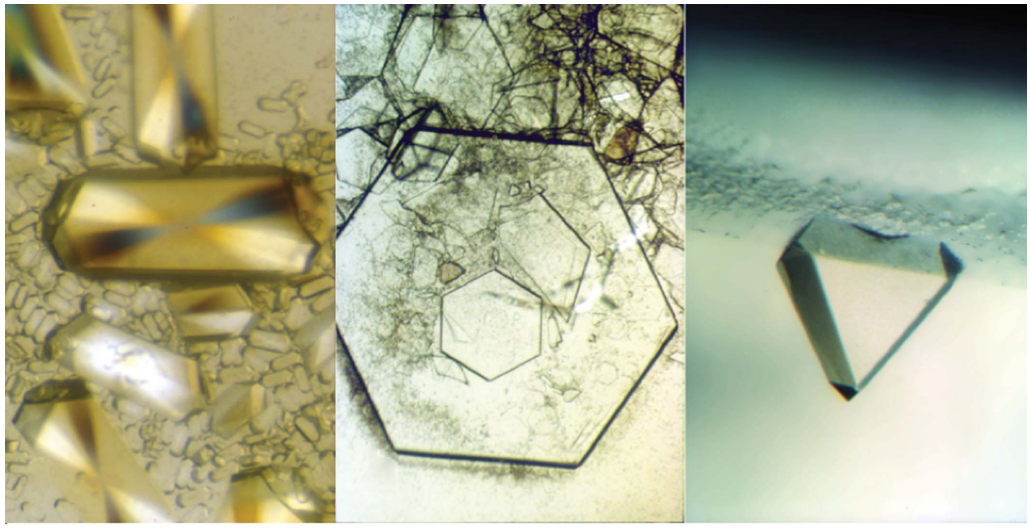

(*a*) (*b*) (*c*)

Figure 1
(*a*) Orthorhombic crystals of STMV with space group *I*222. This is the most common crystal form of STMV and is easily grown from ammonium sulfate at room temperature. (*b*) Monoclinic crystals of STMV with space group *I*2, which are also easily grown from ammonium sulfate, but at 277 K (4°C). The rhombohedral crystal form of STMV, grown from halide salts, is virtually indistinguishable in habit from these monoclinic crystals. (*c*) A cubic crystal of STMV with space group *P*23; cubic crystals can be grown from ammonium sulfate, sodium nitrate and halide salts.

Table 2
Crystal properties of four STMV crystal forms.

Crystal	*I*222 canonical	*I*2 (*C*2)	$P2_12_12$	Ancient cubic†
PDB codes	1a34, 1nia, 4oq8, 4oq9	7m2t	7m57	Not deposited
Crystallization conditions	16%(*w*/*v*) $(NH_4)_2SO_4$, 0.1 *M* phosphate pH 6.0, 298 K	16%(*w*/*v*) $(NH_4)_2SO_4$, 0.1 *M* phosphate pH 6.0, 277 K	16%(*w*/*v*) $(NH_4)_2SO_4$, 0.1 *M* phosphate pH 6.0, 298 K	16%(*w*/*v*) $(NH_4)_2SO_4$, 0.1 *M* Tris pH 8.5, 277 K
Space group	*I*222	*I*2	$P2_12_12$	$P2_13$
a, *b*, *c* (Å)	174.27, 191.77, 202.50,	175.76, 169.86, 244.56	192.08, 202.29, 177.93	257.25, 257.25, 257.25
α, β, γ (°)	90, 90, 90	90, 92.69, 90	90, 90, 90	90, 90, 90
Asymmetric unit	1/4 particle	1/2 particle	1/2 particle	1/3 particle
Resolution (Å)	1.42	46.95–2.71	37.13–4.00	3.3
Particle orientation	On 222 symmetry point	Twofold on *b* axis	Twofold on *c* axis	Threefold on body diagonal
Orientation from canonical	Canonical	32° rotation about *c* axis		11° rotation about threefold (111 direction)
Interparticle distance (Å)	164.43	169.86	166.76	181.9
V_M‡ (Å^3 Da^{-1})	2.43	2.62	2.54	3.06
Solvent volume (%)	49	53	51	60

† Kuznetsov *et al.* (2001). ‡ Matthews (1968).

Table 3
Properties of rhombohedral crystals of STMV grown from sodium chloride and sodium bromide.

PDB code	7m2v	7m39
Crystallization conditions	4%(*w*/*v*) NaCl, 0.1 *M* phosphate pH 6.0, 277 K	5%(*w*/*v*) NaBr, 0.1 *M* phosphate pH 6.0, 277 K
a, *b*, *c* (Å)	165.63, 165.63, 433.32	166.49, 166.49, 435.84
α, β, γ (°)	90, 120.0, 90	90, 120.0, 90
Asymmetric unit	1/3 particle	1/3 particle
Resolution (Å)	55.25–1.80	54.08–2.10
Particle orientation	Threefold on *c* axis	Threefold on *c* axis
Orientation from canonical	80.6° rotation about threefold	80.7° rotation about threefold
Interparticle distance (Å)	166.49	165.75
V_M (Å^3 Da^{-1})	2.50	2.28
Solvent volume (%)	51	46

Table 4
Properties of cubic crystals of STMV grown from sodium chloride.

PDB code	7m3t	5bkn	5bkl
Crystallization conditions	8%(*w*/*v*) NaCl, 0.1 *M* phosphate pH 6.0, 277 K	8%(*w*/*v*) NaCl, 0.1 *M* phosphate pH 6.0, 277 K	8%(*w*/*v*) NaCl, 0.1 *M* phosphate pH 6.0, 277 K
Space group	*P*23	*P*23	*P*23
a, *b*, *c* (Å)	234.05, 234.05, 234.05	234.65, 234.65, 234.65	234.65, 234.65, 234.65
α, β, γ (°)	90, 90, 90	90, 90, 90	90, 90, 90
Asymmetric unit	1/3 particle	1/3 particle	1/3 particle
Resolution (Å)	46.81–3.20	65.08–3.00	78.22–2.94
Particle orientation	Threefold axis on body diagonal	Threefold axis on body diagonal	Threefold axis on body diagonal
Orientation from canonical	80.7° rotation about body diagonal	84.5° rotation about body diagonal	77.9° rotation about body diagonal
Interparticle distance (Å)	165.75	165.46	169.42
V_M (Å^3 Da^{-1})	2.32	2.32	2.32
Solvent volume (%)	47	47	47

belong to space group *I*2 with half a virus particle as the asymmetric unit. The twofold along the *b* crystallographic axis of the *I*222 crystals was preserved, but a slight rotation about this axis destroyed crystallographic symmetry along *a* and *c*.

We further noted, without record, that the crystallization of STMV with other salts and under other conditions often produced diverse habits. One variant was a cubic crystal belonging to space group $P2_13$, grown from ammonium sulfate at pH 8.5, that represented a swollen form of the virus (Kuznetsov *et al.*, 2001).

More recently, we grew additional crystal forms of STMV by substituting sodium chloride, sodium bromide and sodium nitrate for ammonium sulfate at 277 K (Tables 2, 3 and 4). Two distinctly different crystal habits appeared: apex-truncated triangular plates similar to the monoclinic crystals described above (Fig. 1*b*), but with a different unit cell, and large octahedra (Fig. 1*c*), also with a different unit cell to the previous cubic crystals. A fourth habit, grown from ammonium sulfate at 298 K, was that of a small, square plate. These crystals appeared sporadically throughout our studies and were chiefly considered an annoyance. Room-temperature data showed them to be orthorhombic, but with another unit cell that had not previously been found.

2. Materials and methods

Monoclinic crystals were mounted by conventional means in 0.7–0.8 mm quartz capillaries (McPherson, 1982) and X-ray

Table 5
Data-collection and quality statistics for monoclinic, orthorhombic and rhombohedral STMV crystals.

Crystal	*I*2	$P2_12_12$	*R*3, NaCl	*R*3, NaBr
PDB code	7m2t	7m57	7m2v	7m39
X-ray source	Rigaku RU-200	Rigaku RU-200	ALS 8.3.1	ALS 8.3.1
Detector	CCD	CCD	CCD	CCD
Temperature (K)	298	298	173	173
Independent *hkl*	179156	48359	345430	200162
R_{merge}	0.069	0.184	0.084	0.223
Completeness (%)	91.8	81.8	84.0	86.0
Multiplicity	8.4	6.2	4.5	4.6
$CC_{1/2}$	0.99	0.93	0.96	0.94
$\langle I/\sigma(I)\rangle$	12.9	3.00	8.2	4.5
Data reduction	SDMS	*DENZO*	*d*TREK*	*d*TREK*
Scaling	*SCALEPACK*	*DENZO*	*d*TREK*	*d*TREK*
Overall *B* factor (Å^2)	20.1	26.6	13.7	18.0
Twinning (%), twin law	Untwinned	Untwinned	50, $-h-k, k, -l$	50, $-h-k, k, -l$

Table 6
Data-collection and quality statistics for cubic STMV crystals.

PDB code	7m3t	5bkl	5bkn	7m50	5bkq	7m54
X-ray source	ALS 8.3.1	ALS 8.3.1	ALS 8.3.1	ALS 8.3.1	ALS 8.3.1	ALS 8.3.1
Detector	CCD	CCD	CCD	CCD	CCD	CCD
Temperature (K)	173	173	173	173	173	173
Independent *hkl*	69955	86918	85647	159178	45725	33637
R_{merge}	0.12	0.15	0.11	0.17	0.16	0.12
Completeness (%)	99	95	100	86	64	79
Multiplicity	9.55	7.1	6.0	4.8	7.6	5.3
$CC_{1/2}$	0.85	0.83	0.90	0.76	0.87	3.6
$\langle I/\sigma(I)\rangle$	9.9	7.2	21.2	8.4	11.5	7.7
Data reduction	*d*TREK*	*d*TREK*	*d*TREK*	*d*TREK*	*d*TREK*	*d*TREK*
Scaling	*d*TREK*	*d*TREK*	*d*TREK*	*d*TREK*	*d*TREK*	*d*TREK*
Overall *B* factor (Å^2)	34.5	33.9	39.1	28.0	38.5	32.7
Twinning (%), twin law	30%, $l, -k, h$	Untwinned	Untwinned	30%, $l, -k, h$	Untwinned	Untwinned

diffraction data were recorded (approximately 29 years ago) at room temperature using a Rigaku RU-200 generator fitted with a Supper graphite crystal monochromator and operated at 40 kV and 30 mA with twin San Diego Multiwire Systems (SDMS) detectors (Table 2). Images were processed with software provided by SDMS (Howard *et al.*, 1985). Structure amplitudes were obtained by scaling and merging intensities from archived SDMS files and converting them to *POINTLESS* `.mtz` output files using a patch program provided by Duilio Cascio at UCLA. This was followed by the scaling program *AIMLESS* (Evans, 2006, 2011; Evans & Murshudov, 2013) from the *CCP*4 suite (Winn *et al.*, 2011). Reflection data for the orthorhombic $P2_12_12$ crystals used the same source as above but with a CCD detector at room temperature. Data were processed and scaled using *d*TREK* (Pflugrath, 1999). Statistics of reflection data for the monoclinic crystals and the $P2_12_12$ crystals are presented in Table 5.

For the crystals used for the collection of low-temperature data (Tables 5 and 6), STMV was purified (Koszelak *et al.*, 1989) and crystallized by the sitting-drop vapor-diffusion method (McPherson, 1982, 1999) in 24-well Cryschem sitting-drop plates (Hampton Research, Aliso Viejo, California, USA) with ammonium sulfate, sodium chloride, sodium nitrate or sodium bromide as a precipitant (Tables 3 and 4). The protein droplets were 6–8 µl in volume and consisted of equal parts of a 5 mg ml^{-1} virus stock solution and reservoir solution. Crystals usually appeared and grew to full size within one to two weeks. The crystals were mounted in cryo-loops, submerged in mother liquor (minus virus) containing 20% PEG 3350 and 30% MPD for 30 s and flash-cooled on the goniometer in a nitrogen cold stream. Data were collected on beamline 8.3.1 at the Advanced Light Source (ALS) at 173 K using an ADSC CCD detector at a wavelength of 1.06 Å. The crystal-to-detector distance was 204.8 mm. Images were obtained as 0.33° ω scans. The data were processed with *d*TREK* (Pflugrath, 1999). Data-collection and scaling statistics for each crystal studied are shown in Tables 5 and 6.

Structures were determined by molecular replacement using *Phaser* (McCoy *et al.*, 2005; Storoni *et al.*, 2004; Read, 2001). For the monoclinic and orthorhombic crystals, asymmetric units consisting of half particles were constructed from PDB entry 4nia by rotating about a twofold axis. For the cubic and rhombohedral crystals, an asymmetric unit consisting of one third of a particle was constructed from PDB entry 4oq8 by the addition of an additional pentamer of protein subunits with their associated RNA.

Refinements were initially carried out for all crystal forms using *REFMAC*5 (Murshudov *et al.*, 2011), but all structures were refined to finalized models using *phenix.refine* (Afonine *et al.*, 2012) from the *Phenix* suite (Liebschner *et al.*, 2019). The final refinement statistics are shown in Tables 7 and 8. $2mF_o - DF_c$ Fourier and $mF_o - DF_c$ difference Fourier maps were computed and displayed with *Coot* version 9.1 (Emsley *et al.*, 2010).

Table 7
Model and refinement statistics for monoclinic, orthorhombic and rhombohedral crystals of STMV.

Crystal, salt	*I*2, $(NH_4)_2SO_4$	$P2_12_12$, $(NH_4)_2SO_4$	*R*3 (*H*3), NaCl	*R*3 (*H*3), NaBr
PDB entry	7m2t	7m57	7m2v	7m39
Starting model	PDB entry 4oq8, twofold expanded to 1/2 virus particle	PDB entry 4oq8, twofold expanded to 1/2 virus particle	PDB entry 4oq8, expanded to 1/3 virus particle	PDB entry 4oq8, expanded to 1/3 virus particle
Model: protein, RNA	30 protein subunits: 147 amino acids (1155 atoms), 20 nucleotides (414 atoms)	30 protein subunits: 147 amino acids (1155 atoms), 20 nucleotides (414 atoms)	30 protein subunits: 147 amino acids (1155 atoms), 20 nucleotides (414 atoms)	30 protein subunits: 147 amino acids (1155 atoms), 20 nucleotides (414 atoms)
Refinement program	*REFMAC* (initial), *phenix.refine* (final)	*REFMAC* (initial), *phenix.refine* (final)	*REFMAC* (initial), *phenix.refine* (final)	*REFMAC* (initial), *phenix.refine* (final)
Resolution (Å)	2.7	4.0	1.8	2.1
R_{work}	0.13	0.20	0.13	0.17
R_{free}	0.18	0.24	0.16	0.20
R.m.s.d., bond lengths (Å)	0.003	0.002	0.006	0.003
R.m.s.d., bond angles (°)	0.53	0.45	0.69	0.49
Clashscore	2.0	4.0	7.0	5.0
Ramachandran outliers (%)	0.20	0.00	0.30	0.49
Rotamer outliers (%)	0.10	0.10	0.20	0.10
No. of waters	2797	16	5564	4465
Ligands	6 PO_4^{3-}, 5 SO_4^{2-}	6 PO_4^{3-}, 2 SO_4^{2-}	13 Cl^-, 4 PO_4^{3-}, 8 Mg^{2+}	191 Br^-, 8 Mg^{2+}

Table 8
Model and refinement statistics for cubic crystals of STMV.

Crystal, salt	*P*23, NaCl	*P*23, NaCl	*P*23, NaCl	*P*23, $(NH_4)_2SO_4$	*P*23, $NaNO_3$	*P*23, NaBr
PDB code	5bkl	7m3t	5bkn	7m50	5bkq	7m54
Starting model	PDB entry 4oq8 expanded to 1/3 virus particle	PDB entry 4oq8 expanded to 1/3 virus particle	PDB entry 4oq8 expanded to 1/3 virus particle	PDB entry 4oq8 expanded to 1/3 virus particle	PDB entry 4oq8 expanded to 1/3 virus particle	PDB entry 4oq8 expanded to 1/3 virus particle
Model: protein/RNA	30 protein subunits: 147 amino acids (1155 atoms), 20 nucleotides (414 atoms)	30 protein subunits: 147 amino acids (1155 atoms), 20 nucleotides (414 atoms)	30 protein subunits: 147 amino acids (1155 atoms), 20 nucleotides (414 atoms)	30 protein subunits: 147 amino acids (1155 atoms), 20 nucleotides (414 atoms)	30 protein subunits: 147 amino acids (1155 atoms), 20 nucleotides (414 atoms)	30 protein subunits: 147 amino acids (1155 atoms), 20 nucleotides (414 atoms)
Refinement program	*REFMAC* (initial), *phenix.refine* (final)	*REFMAC* (initial), *phenix.refine* (final)	*REFMAC* (initial), *phenix.refine* (final)	*REFMAC* (initial), *phenix.refine* (final)	*REFMAC* (initial), *phenix.refine* (final)	*REFMAC* (initial), *phenix.refine* (final)
Resolution (Å)	2.9	3.2	3.0	2.3	3.2	3.8
R_{work}	0.22	0.22	0.20	0.22	0.21	0.24
R_{free}	0.25	0.25	0.24	0.25	0.25	0.29
R.m.s.d., bond lengths (Å)	0.004	0.003	0.002	0.002	0.003	0.004
R.m.s.d., bond angles (°)	0.72	0.55	0.60	0.55	0.51	0.55
Clashscore	7.0	4.0	3.0	4.0	3.0	5.0
Ramachandran outliers (%)	0.50	0.10	0.30	0.49	0.40	0.60
Rotamer outliers (%)	0.10	0.10	0.40	0.10	0.30	0.40
No. of waters	859	1058	619	4318	1583	580
Ligands	4 PO_4^{3-}, 28 Cl^-, 14 Mg^{2+}	7 PO_4^{3-}, 15 Cl^-, 6 Mg^{2+}	25 Cl^-, 14 Mg^{2+}	6 PO_4^{3-}, 1 Cl^-, 5 Mg^{2+}, 6 SO_4^{2-}	102 NO_3^-, 8 Mg^{2+}	182 Br^-, 3 Cl^-, 6 Ca^{2+}, 9 Mg^{2+}

Of the four crystal forms described here, two crystals, the monoclinic and orthorhombic crystals, were not twinned (Table 5). Rhombohedral crystals grown from sodium chloride and sodium bromide were both twinned and two cubic crystals, one grown from sodium chloride and the other from ammonium sulfate, were also twinned (Table 6). All were twinned about a crystallographic threefold axis. The *I*2 crystals were solved after doubling the quarter-particle asymmetric unit of the canonical *I*222 crystals (PDB entry 4nia) to produce an appropriate model. *Phaser* (McCoy *et al.*, 2005; Read, 2001; Storoni *et al.*, 2004; McCoy *et al.*, 2007) was used to orient and position the asymmetric unit in the *I*2 cell, and subsequent refinement was accomplished as described in Table 7. The low *R* values and robust geometry obtained were undoubtedly a consequence of the near-congruence of the final *I*2 model with the starting *I*222 model (PDB entry 4oq8) refined at 1.42 Å resolution (Larson *et al.*, 2014). All of the RNA segments appeared to be virtually identical and as well ordered as in the *I*222 crystals. If synchrotron sources and pixel-array detectors had been available at the time that the *I*2 crystal data were collected (1992), it seems likely that the resolution of these crystals would have approached or equalled that of the flash-cooled *I*222 crystals (Larson *et al.*, 2014).

Only low-resolution reflections could be recorded for the $P2_12_12$ crystals, owing to both room-temperature data collection using a laboratory source and the small size and marginal quality of the crystals. Nonetheless, the structure, a half-particle placed by *Phaser*, refined without difficulty (Table 7). Again, the overall quality of the refinement was surely a reflection of the starting model. The RNA segments were present and although not defined in detail at 4.0 Å resolution, suggested no difference from those seen in the *I*222 and *I*2 crystals.

Data were recorded from flash-cooled rhombohedral crystals grown from sodium chloride and from sodium bromide at resolutions of 1.8 and 2.1 Å, respectively, from cubic crystals grown from sodium chloride and sodium nitrate, and from a serendipitous cubic crystal that appeared from ammonium sulfate (Tables 3 and 4). The diffraction intensities for the cubic crystals ranged in resolution from 2.3 to 3.2 Å (Tables 5 and 6). A data set was also obtained for a cubic crystal grown from sodium bromide, but only at 4.0 Å resolution (Table 6). The data from the rhombohedral and some of the cubic crystals were predicted by *phenix.xtriage* from the *Phenix* suite (Liebschner *et al.*, 2019) to arise from twinned crystals. The twinned cubic crystals were predicted (Padilla & Yeates, 2003) to be about 35%/65% twins (twin law l, $-k$, h), while the rhombohedral crystals, which were initially assumed to belong to space group $R32$, were indeed perfect 50% twins in space group $R3$ (twin law $-h-k$, k, $-l$). With respect to the canonical $I222$ model, the crystals were twinned by virtue of rotations from dyads of 32° about the unique axis in the rhombohedral crystals and by rotations that varied over a 9° range about the threefold body diagonals of the cubic crystals.

Principally because of some disorder in the RNA segments, particularly at their termini, and multiple paths for some amino-terminal peptides (amino acids 1–16) refinement of the cubic crystals was somewhat problematic, and the final R factors were higher than we obtained for well ordered $I222$ and $I2$ crystals. Ramachandran outliers (Tables 7 and 8) were almost exclusively confined to the partially disordered, extended amino-terminal peptides. Isotropic displacement factors were used and TLS refinement was included, but no NCS or icosahedral restraints were applied. The inclusion of NCS restraints in several tests indicated that they had little influence on the refinement.

3. Results

3.1. Crystals grown from ammonium sulfate, sodium chloride, sodium bromide and sodium nitrate and their differences: the presence or absence of ordered RNA

There is a striking difference between the rhombohedral crystals grown from sodium chloride and those grown from sodium bromide, although both exhibit the same symmetry and virtually the same unit-cell parameters (Table 3). The diffraction intensities of both extend to relatively high resolution, 1.8 Å for the sodium chloride-grown crystals and 2.1 Å for those grown from sodium bromide, and both refine well, although both are twinned, to respectable R values and good geometry (Table 8). The pronounced difference is that while the sodium chloride-grown crystals clearly exhibited all of the ordered RNA seen previously in $I222$ and $I2$ crystals, those grown from sodium bromide exhibited none. In the latter case, the RNA either was lost entirely from the virions, or was still within them but was totally disordered.

This pattern was repeated in the cubic crystals. Electron-density maps for three independent data sets collected from crystals in space group $P23$ grown from sodium chloride, with different particle rotations that vary from 77° to 85° about the body diagonals, show that the RNA is present and ordered within the capsids. A crystal also belonging to space group $P23$ with the same unit-cell parameters, but grown from ammonium sulfate, also showed the RNA to be intact and ordered within the capsids. The cubic crystals grown from sodium bromide, although of low resolution, nonetheless exhibited no ordered RNA, consistent with what was observed in the rhombohedral crystals. In addition, cubic crystals grown using sodium nitrate also appeared to be vacant of RNA.

Table 9
Ions on symmetry axes in all STMV crystal forms.

Crystals, salts	PDB code	Ions on fivefold axes: Outside capsid	Ions on fivefold axes: Inside capsid	Ions on threefold axes
$I222$, $(NH_4)_2SO_4$†	4oq8	None	PO_4^{3-}	None
$I2$, $(NH_4)_2SO_4$	7m2t	None	PO_4^{3-}	None
$P2_12_12$, $(NH_4)_2SO_4$	7m57	None	PO_4^{3-}	None
$R3$, NaCl	7m2v	Cl^-	PO_4^{3-}	None
$R3$, NaBr	7m39	Br^-	Br^-	Br^-
Cubic, NaCl (1)	7m3t	Cl^-	PO_4^{3-}	None
Cubic, NaCl (2)	5bkn	Cl^-	PO_4^{3-}	None
Cubic, NaCl (3)	5bkl	Cl^-	PO_4^{3-}	None
Cubic, $(NH_4)_2SO_4$	7m50	None	PO_4^{3-}	None
Cubic, $NaNO_3$	5bkq	NO_3^-	NO_3^-	NO_3^-
Cubic, NaBr	7m54	Br^-	Br^-	Br^-
$I222$, NaI soak‡		None	I^-	None

† Larson *et al.* (2014). ‡ Data were collected to only 5 Å resolution. The structure has not been deposited in the PDB.

3.1.1. Anion-binding patterns in the various crystals: the icosahedral fivefold axes. STMV crystals exhibited a variety of anion-binding patterns depending on the salts from which they were crystallized (Table 9). The investigation presented here reveals a more complicated picture of what transpires at the viral fivefold vertices and within their corresponding channels. In both rhombohedral and cubic crystals grown from sodium chloride, the phosphate ion seen on the fivefold axis and slightly inside the capsid (Larson *et al.*, 2014) in crystals grown from ammonium sulfate ($I222$, $I2$ and $P23$) continues to be present. There is, however, a second anion also on the fivefold axis. This second ion is slightly outside the capsid (Fig. 2). A distance of 5.0 Å separates the two ions. The chloride ion outside the capsid exhibits a lower occupancy, perhaps 75% of that of the phosphate ion inside the capsid.

In crystals, both rhombohedral and cubic, grown from sodium bromide, there are again two anions on a fivefold axis, as in the sodium chloride-grown crystals, but in these crystals both anions are bromides; the phosphates are apparently displaced by bromide ions. For the cubic crystal grown from sodium nitrate, there are two nitrate ions on the fivefold axes rather than bromide ions. Nitrate, as well as bromide, also displaces the interior phosphate on the fivefold axis.

Identification of the various ions was not difficult owing to their differing ionic radii and total electron complement. There were other useful features. For example, bromide ions were almost always accompanied by a hydrogen-bonded water molecule (2.9 Å) that produced a 'tail' on the ion, as shown in Fig. 3. In addition, most bromide ions were closely associated

with the guanidinium moiety of an arginine residue, as also seen in Fig. 3. Chlorides were distinguishable from waters by their greater radius and their appearance in difference Fourier maps with peak heights generally exceeding 5σ. Phosphate groups have a radius of nearly 2.5 Å and a high electron count, and nitrate ions are planar and appear in difference maps with appropriately flattened shapes.

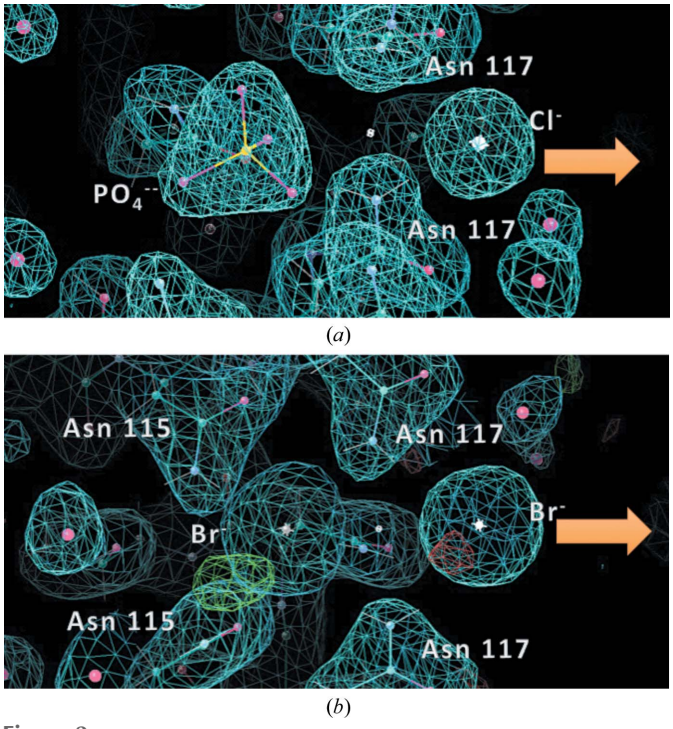

Figure 2
(*a*) The fivefold channel of the virion in a crystal grown from sodium chloride. On the left is a phosphate ion, superimposed on its electron density, slightly within the capsid and occupying the same position as it does in crystals grown from ammonium sulfate. Slightly outside the capsid is a chloride ion 5 Å away and also on the fivefold axis. No such ion is present in crystals grown from ammonium sulfate. (*b*) Two bromide ions replace both the phosphate and chloride ions shown in (*a*) in crystals grown from sodium bromide. They are in the same locations as the two nitrate ions shown in Fig. 4.

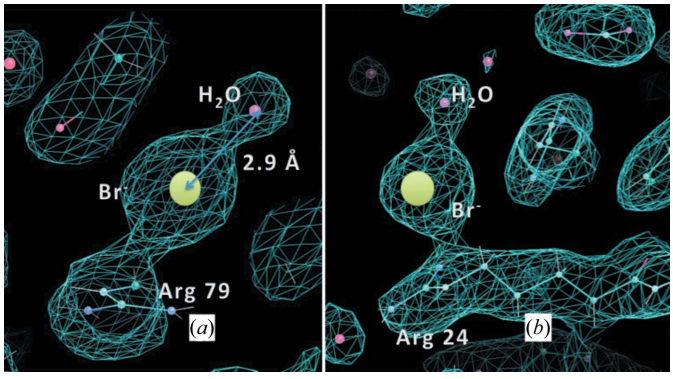

Figure 3
Bromide ions in the STMV crystals grown from sodium bromide invariably have a water molecule hydrogen bonded to the ion at a distance of 2.9 Å, as shown in both (*a*) and (*b*). The bromide is frequently adjacent to the guanidinium moiety of an arginine residue, as shown here.

3.1.2. Anion-binding patterns of the various crystals: the icosahedral threefold axes. In addition to their occurrence on viral fivefold axes, bromide and nitrate ions were also found on the viral threefold axes, just inside the capsid. The threefold-associated ions must have entered the virion upon exposure to sodium nitrate or sodium bromide during crystallization. The binding environment of a bromide at a threefold vertex is shown in Fig. 4. Its nearest amino acids from the protein subunits are threefold symmetry-related Asn129 and symmetry-related Ser128 residues. Binding seems to produce no observable perturbation of the local capsid structure. In none of the crystals grown from sodium chloride or ammonium sulfate was an ion of any kind bound at the threefold vertex.

3.1.3. A break in the icosahedral symmetry. A curious observation emerged from the refinement of the *R*3 and *P*23 crystals that was not apparent in the other crystal forms, an observation that we have difficulty understanding or explaining. The protein capsid has exact icosahedral symmetry, and its structure is presumed to be physically 60-fold averaged when it enters the crystal lattice. There is unlikely to be any preferred orientation, since the orientation in the lattice is again assumed to be wholly dependent on the icosahedral virus surface structure. There is no compelling reason to believe that the orientation of the asymmetric, single-stranded RNA molecule that inhabits the virus interior influences the particle orientation in the crystal lattice.

The expectation, therefore, is that exact icosahedral symmetry, although not explicitly imposed, should prevail in electron-density maps, and that the density representing the RNA (mostly helical) segments centered on icosahedral twofold axes, and associated with each dimer of protein subunits, would be identical. The same should be true of the amino-terminal strands otherwise unseen. This does not seem to be the case. While strong icosahedral symmetry prevails, it

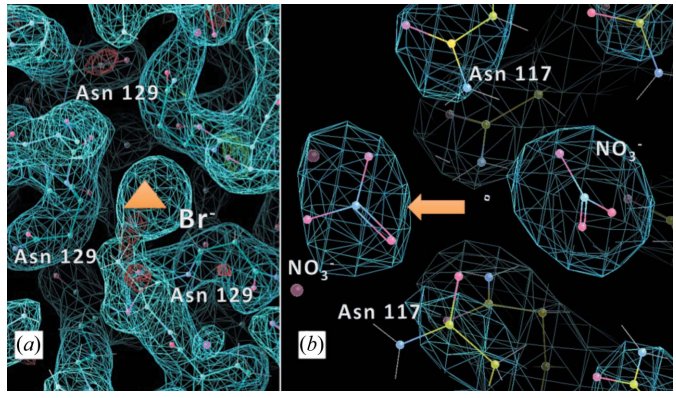

Figure 4
(*a*) The electron density of a bromide ion is situated exactly on an icosahedral threefold axis of the protein capsid. (*b*) Two nitrate ions are shown, superimposed on their electron density, aligned along an icosahedral fivefold axis at a fivefold vertex. The ion on the right is slightly inside the capsid and replaces the phosphate ion that is present in crystals grown from ammonium sulfate and sodium chloride. The nitrate ion 5 Å to the left is slightly outside the capsid. Some asparagine residues that form the fivefold 'gate' are also seen.

is flawed, particularly at or near RNA-segment termini. Thus, the RNA segments at the icosahedral dyads vary somewhat in appearance. Some RNA segments exhibit as many as 12 nucleotides, while others are as short as seven. In addition, the otherwise absent amino-terminal tails (amino acids 1–16) of each protein subunit often permit extension of the backbone by many residues for some protein subunits and not at all for others.

The exact icosahedral symmetry in the interior of the virus particle appears to be broken. RNA strands and amino-terminal strands at each icosahedral twofold appear individually and are differently affected. To be consistent with the electron density, some had to be shortened and some lengthened. Extensions of RNA strands at helix ends were sometimes evident as, even more so, were extensions of some amino-terminal strands. It seems difficult to avoid the suspicion that the RNA molecule in the virus interior does indeed affect the way that a virus particle enters the crystal lattice; that is, it may indeed impose, perhaps only slightly, some preferred orientation.

3.1.4. Amino-terminal strand organization. Crystals, both rhombohedral and cubic, that were grown from sodium bromide or sodium nitrate revealed capsids devoid of ordered RNA. The helical RNA segments previously found at icosahedral dyads had detached from the capsid proteins. One consequence was that the amino-terminal strands of some subunits, as noted above, appeared to be ordered beyond their usual (in the presence of ordered RNA) visible length. In orthorhombic, monoclinic and both rhombohedral and cubic crystals grown from sodium chloride, with some exceptions, the final amino acid seen at the amino-terminal end was Ser17 or Asp16. In some rare instances in RNA-absent capsids the amino-terminal strand of some protein subunits could sometimes be followed in the electron density to Lys3, and often to Lys11 or Thr13. Fig. 5 shows an exceptional amino-terminus of a subunit of a virion where the final visible amino acid is Lys3.

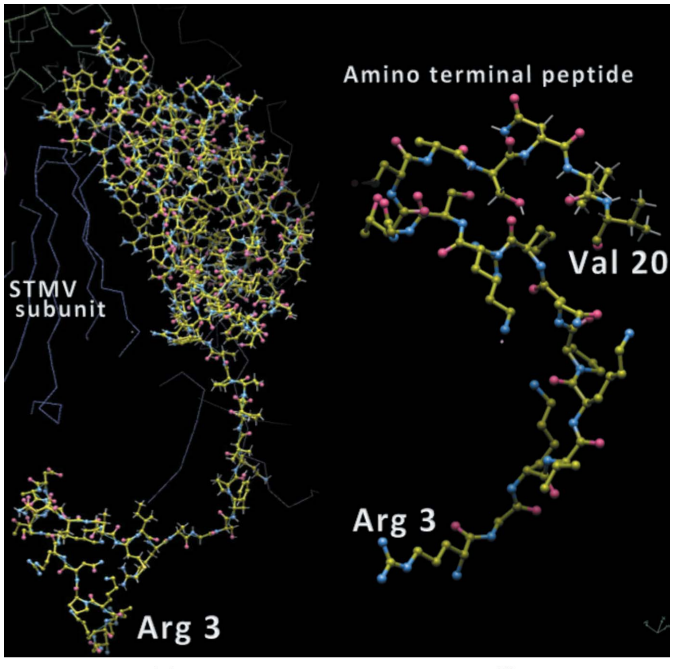

(*a*) (*b*)

Figure 5
An example of the extended amino-terminal tails that were observed for some protein capsid subunits, particularly in crystals grown from sodium bromide or sodium nitrate where the RNA has been released from the capsid protein. The subunit in (*a*) contains amino acids from Arg3 to the carboxy-terminus at 159; only Met1 and Lys2 are unobserved. (*b*) A more detailed image of the extended tail, amino acids 2–20, is shown.

In general, the tracks of the amino-terminal strands from the various capsid subunits assume somewhat different paths, and often alternate paths are suggested even for some individual strands. An example where the strands are more organized is from a cubic crystal grown from sodium nitrate (PDB entry 5bkq). The threefold-related capsid subunits *E*, *J* and *O* (PDB designations) all allowed independent tracing of their amino-terminal strands to Lys11 or beyond. The strands arrange themselves with approximate threefold symmetry about the triad as they protrude into the interior of the capsid. The courses of the three strands are different in detail, but they suggest a likely arrangement of terminal strands throughout the virion. The amino-terminal strands are rich in positively charged amino acids and their diverse paths in RNA-containing virions are undoubtedly determined in detail by their interactions with local RNA strands, which vary from icosahedral twofold to icosahedral twofold axis. In the absence of RNA, the amino-terminal peptides are free to reorganize or restructure about threefold axes.

3.1.5. Ion channels at the fivefold axes. An examination of icosahedral viruses (Natarajan *et al.*, 2005) would show that there is very seldom an opening or channel to the virus interior at sixfold (for $T > 1$ icosahedra) or threefold vertices. Generally, the subunits converge structurally and pack to occlude any pathway. This is not true of viral fivefold vertices, where an opening is often present that could allow passage along fivefold symmetry axes. Furthermore, there is frequently an ion observed bound at the vertex or in the channel; this is always the case in STMV. These channels, in general, provide the most attractive possibilities for the exchange of ions and small molecules between the interior and the exterior of virions. No specific functions have been assigned to the fivefold axial channels, but their ubiquity suggests that they may play a role in the infection cycle of the viruses, possibly in the assembly or the decapsidation of the nucleic acid. The latter, in particular, could be triggered by exterior changes in the ionic or small-molecule environment of the viruses upon infection of tobacco cells.

The similarities of the fivefold channels in icosahedral viruses to ion channels has previously been noted and discussed (Kalko *et al.*, 1992), but based on a then limited set of icosahedral viruses. Virus structures determined later have, however, been consistent with the conclusions of this earlier study. This investigation did not include STMV, which at 1.42 Å resolution provides the most detailed picture of such a fivefold channel and a channel that is seen in the presence of many different ions (Table 9).

In the canonical, orthorhombic crystals of STMV, we found in our earliest analyses (Larson *et al.*, 1993, 1998) that the fivefold vertices were relatively open and were occupied by an

ion. Because the crystals were grown from ammonium sulfate solutions [15–20%(*w*/*v*)] we presumed the ion to be sulfate. Subsequent data and higher resolution analysis (Larson *et al.*, 2014) persuaded us that the ion was more likely to be phosphate. It can possibly be either.

Given the evidence, in part, from the threefold-associated bromide and nitrate ions that some anions can pass in and out of the capsid, the curious arrangement of two ions at the fivefold vertices and the observation that there are no other suitable channels or passages that would allow transport through the capsid, the channels along the fivefold axes might be considered to be some sort of ion channel. This, as already noted, is also consistent with the conclusions of an earlier study (Kalko *et al.*, 1992)

The linear arrangement of anions along fivefold axes (Figs. 2, 4 and 6) is suggestive of this hypothesis; the interior anion is the more stable based on occupancies and binding environment, while the outside anion possibly represents an approaching or exiting ion. An important consideration is the detailed structure at the vertex and the channel and the electrostatic environment that it might impose on the ions therein. As seen in Fig. 6(*c*), the opening through the vertex is slightly too narrow to allow the passage of bromide ions (ionic radius 1.85 Å; Marcus, 1988) or even chloride ions (ionic radius 1.75 Å; Marcus, 1988). For the channel to allow passage there must be some conformational changes in the amino-acid side chains that surround, ostensibly with fivefold symmetry, the channel.

The restrictive, structural annulus that serves as a gateway consists of two, fivefold-symmetrical rings of asparagine side chains (Larson *et al.*, 1998), with their ten amide N atoms interacting most closely with the two anions and being responsible for their binding (Fig. 7). Little change in the asparagine side-chain conformations would be necessary, however, to open the channel and allow the passage of an anion. Furthermore, the fivefold arrangements of the two rings are icosahedrally symmetric, not crystallographically determined, and thus the side chains could move, or not move at all, independently of one another to open the gate. An additional consideration is that the ions are doubtlessly hydrated, and this would significantly enlarge the effective ionic radius were the ions not first dehydrated preceding entry or exit (Collins, 2019; Kiriukhin & Collins, 2002).

The most intriguing feature of the ten-asparagine gateway lies in its potential to effect dynamic events within the channel. The ten amide groups that interact with an anion contain a carbonyl O atom carrying a partial negative charge and an amide N atom carrying a partial positive charge, with the two being separated by 2.25 Å. These dipoles are free to move and rotate at the ends of alkyl arms of modest length, and as they reorient they will produce changing, local electrostatic fields in the channel. Because they can reorient independently of one another, there are enormous possibilities for an ever-changing electrostatic environment about the ions in the channel. Fluctuating fields could provide the motive forces to propel ions in and out of a virion.

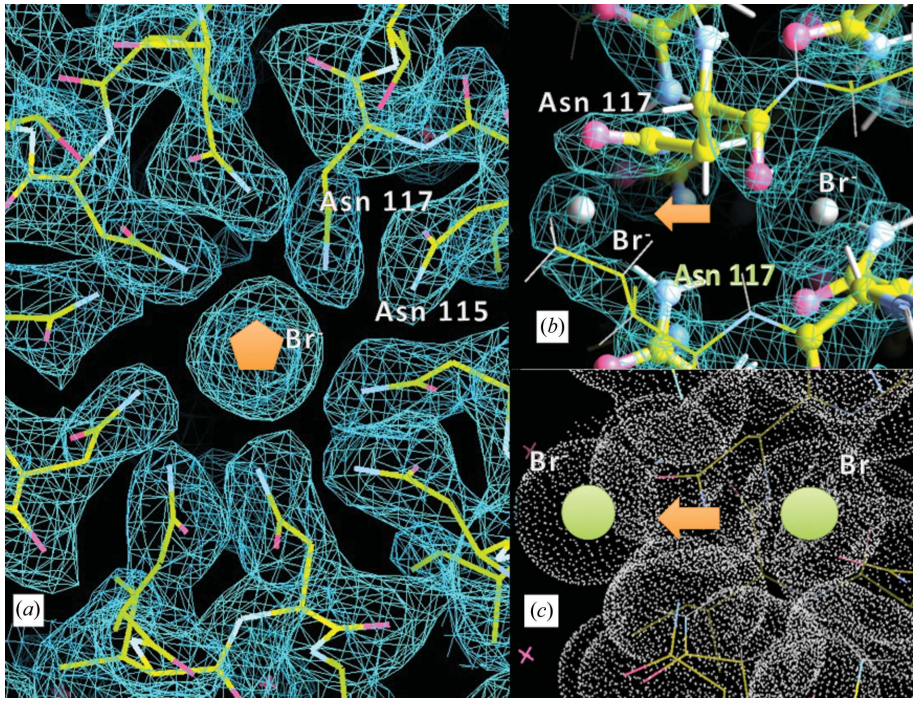

Figure 6
The fivefold gateway at an icosahedral fivefold vertex is shown in (*a*) with the two rings comprised of ten asparagine residues surrounding a central anion, here a bromide. The structure is shown superimposed upon its electron density. (*b*) A view 90° to that in (*a*) showing two bromide anions aligned along the fivefold axis and surrounded by asparagine side chains. (*c*) The arrangement of ions and residues is the same as in (*b*) but atoms have been replaced by dot spheres of appropriate atomic radius. The image in (*c*) emphasizes the crowded nature of the 'gateway' and its impassibility to anions unless there are local conformational changes in the asparagine side chains.

3.1.6. Crystals suffused with sodium iodide. An interesting case is provided by crystals of STMV (space group *I*222) exposed to high concentrations of sodium iodide. We were unable to grow crystals directly from sodium iodide, but orthorhombic crystals grown from ammonium sulfate could be transferred to solutions containing a high concentration of sodium iodide. Difference Fourier syntheses (McPherson, 1987) showed that no iodide ions could be found at the threefold vertices where bromide and nitrate ions were found. In addition, only one iodide ion was found on the fivefold axes, and this was at the usual location of the phosphate ion just inside the capsid (Fig. 7). The iodide also succeeded in displacing the phosphate and entering the capsid. No second anion was present just outside the capsid.

Weaker binding properties are likely to explain the absence of a second, iodide ion on the fivefold axis, and its greater ionic radius, and hence the impedance in diffusion, probably also accounts for its absence at the threefold positions. The replacement of the sulfate or phosphate ion at the fivefold vertex does, however, imply that in spite of its greater size, even iodide can traverse the asparagine gateway and displace a phosphate ion.

3.1.7. Crystals grown from sodium nitrate: a possible mechanism for RNA decapsidation. What may be the most physiologically interesting and intriguing finding was the result for crystals grown from sodium nitrate. The capsids in these crystals were also devoid of RNA, or at least ordered RNA. It should be noted that while some chloride ions were identified in crystals grown from sodium nitrate, a large number of bromide and nitrate ions were found in their crystals, frequently replacing the phosphate groups of the RNA in sodium chloride-grown and ammonium sulfate-grown crystals. Bromide and nitrate ions also replaced the phosphate ions found previously at the fivefold vertices of crystals grown from ammonium sulfate (Fig. 3). It seems clear from these results that bromide and nitrate ions effectively compete away phosphate groups and produce disruption of the protein–RNA interactions within the capsids.

It seems very unlikely, and there is no evidence, that bromide ions play any role in the RNA-decapsidation process of the virus *in vivo*, although they may *in vitro*, for example during crystallization. The concentration of bromide is almost negligible inside normal tobacco cells. This is not true of nitrate ions, however. In normal tobacco-leaf cells, the amount of nitrate is estimated to be between 1.5 and 5 g per kilogram (Hord *et al.*, 2009; Sims *et al.*, 1970). This equates to somewhere between 30 and 80 m*M*, and possibly much higher if only the cytoplasmic fraction of the leaves is considered.

The mechanism by which STMV effects decapsidation when it enters a tobacco cell is not known, although some light has been shed by AFM and biophysical investigations (Kuznetsov *et al.*, 2010). We speculate of course, but the results here suggest that disruption of internal RNA, release from its protein bondage and possible decapsidation may occur as a consequence of its sudden exposure to the nitrate ions in the interior of tobacco cells.

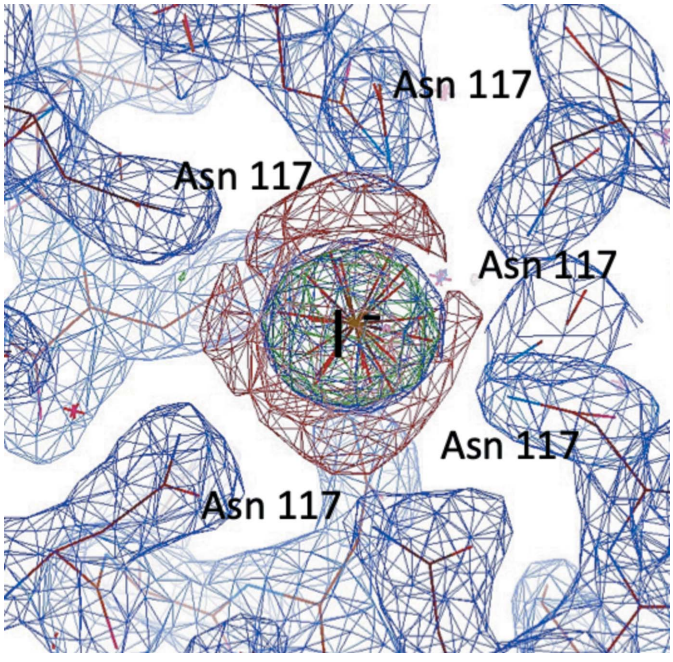

Figure 7
An image from a $2mF_o - DF_c$ Fourier synthesis of a crystal grown from ammonium sulfate that was transferred into a solution containing 15%(*w*/*v*) sodium iodide lacking any phosphate or sulfate. The phosphate ion (ionic radius 2.45 Å, 49 electrons, 1.95 e Å^{-3}) that would normally be present is replaced by an iodide ion (atomic radius 2.06 Å, 55 electrons, 3.10 e Å^{-3}). This is clear from the distribution of positive (green) and negative (red) difference density within the anion.

Acknowledgements

The author wishes to thank Mr John Day who assisted in the early data collection and Dr Steven Larson who processed the X-ray data and performed initial evaluations.

References

Afonine, P. V., Grosse-Kunstleve, R. W., Echols, N., Headd, J. J., Moriarty, N. W., Mustyakimov, M., Terwilliger, T. C., Urzhumtsev, A., Zwart, P. H. & Adams, P. D. (2012). *Acta Cryst.* D**68**, 352–367.
Archer, E. J., Simpson, M. A., Watts, N. J., O'Kane, R., Wang, B., Erie, D. A., McPherson, A. & Weeks, K. M. (2013). *Biochemistry*, **52**, 3182–3190.
Ban, N., Larson, S. B. & McPherson, A. (1995). *Virology*, **214**, 571–583.
Ban, N. & McPherson, A. (1995). *Nat. Struct. Mol. Biol.* **2**, 882–890.
Brünger, A. T., Adams, P. D., Clore, G. M., DeLano, W. L., Gros, P., Grosse-Kunstleve, R. W., Jiang, J.-S., Kuszewski, J., Nilges, M., Pannu, N. S., Read, R. J., Rice, L. M., Simonson, T. & Warren, G. L. (1998). *Acta Cryst.* D**54**, 905–921.
Brünger, A. T., Kuriyan, J. & Karplus, M. (1987). *Science*, **235**, 458–460.
Caspar, D. L. D. & Klug, A. (1962). *Cold Spring Harb. Symp. Quant. Biol.* **27**, 1–24.
Collins, K. D. (2019). *Q. Rev. Biophys.* **52**, e11.
Day, J., Kuznetsov, Y. G., Larson, S. B., Greenwood, A. & McPherson, A. (2001). *Biophys. J.* **80**, 2364–2371.
Day, J. & McPherson, A. (1992). *Protein Sci.* **1**, 1254–1268.
DeLucas, L. J., Smith, C. D., Carter, D. C., Twigg, P., He, X. M., Snyder, R. S., Weber, P. C., Schloss, J. V., Einspahr, H. M., Clancy, L. L., McPherson, A., Koszelak, S., Vandonselaar, M. M., Prasad,

L., Quail, J. W., Delbaere, L. T. & Bugg, C. E. (1992). *Adv. Space Res.* **12**, 393–400.
Emsley, P., Lohkamp, B., Scott, W. G. & Cowtan, K. (2010). *Acta Cryst.* D**66**, 486–501.
Evans, P. (2006). *Acta Cryst.* D**62**, 72–82.
Evans, P. R. (2011). *Acta Cryst.* D**67**, 282–292.
Evans, P. R. & Murshudov, G. N. (2013). *Acta Cryst.* D**69**, 1204–1214.
Felden, B. (1994). PhD thesis. IBMC, Strasbourg, France.
Freddolino, P. L., Arkhipov, A. S., Larson, S. B., McPherson, A. & Schulten, K. (2006). *Structure*, **14**, 437–449.
Hord, N. G., Tang, Y. & Bryan, N. S. (2009). *Am. J. Clin. Nutr.* **90**, 1–10.
Howard, A. J., Nielsen, C. & Xuong, N. H. (1985). *Methods Enzymol.* **114**, 452–472.
Kalko, S. G., Cachau, R. E. & Silva, A. M. (1992). *Biophys. J.* **63**, 1133–1145.
Kiriukhin, M. Y. & Collins, K. D. (2002). *Biophys. Chem.* **99**, 155–168.
Koszelak, S., Dodds, J. A. & McPherson, A. (1989). *J. Mol. Biol.* **209**, 323–325.
Koszelak, S., Leja, C. & McPherson, A. (1996). *Biotechnol. Bioeng.* **52**, 449–458.
Kuznetsov, Y. G., Dowell, J. J., Gavira, J. A., Ng, J. D. & McPherson, A. (2010). *Nucleic Acids Res.* **38**, 8284–8294.
Kuznetsov, Y. G., Larson, S. B., Day, J., Greenwood, A. & McPherson, A. (2001). *Virology*, **284**, 223–234.
Land, T. A., Malkin, A. J., Kutznesov, Y. G., McPherson, A. & De Yoreo, J. J. (1996). *J. Cryst. Growth*, **166**, 893–899.
Larson, S. B., Day, J., Greenwood, A. & McPherson, A. (1998). *J. Mol. Biol.* **277**, 37–59.
Larson, S. B., Day, J. S. & McPherson, A. (2014). *Acta Cryst.* D**70**, 2316–2330.
Larson, S. B., Koszelak, S., Day, J., Greenwood, A., Dodds, J. A. & McPherson, A. (1993). *Nature*, **361**, 179–182.
Larson, S. B. & McPherson, A. (2001). *Curr. Opin. Struct. Biol.* **11**, 59–65.
Liebschner, D., Afonine, P. V., Baker, M. L., Bunkóczi, G., Chen, V. B., Croll, T. I., Hintze, B., Hung, L.-W., Jain, S., McCoy, A. J., Moriarty, N. W., Oeffner, R. D., Poon, B. K., Prisant, M. G., Read, R. J., Richardson, J. S., Richardson, D. C., Sammito, M. D., Sobolev, O. V., Stockwell, D. H., Terwilliger, T. C., Urzhumtsev, A. G., Videau, L. L., Williams, C. J. & Adams, P. D. (2019). *Acta Cryst.* D**75**, 861–877.
Malkin, A. & McPherson, A. (1993). *J. Cryst. Growth*, **128**, 1232–1235.
Malkin, A. J., Cheung, J. & McPherson, A. (1993). *J. Cryst. Growth*, **126**, 544–554.
Marcus, Y. (1988). *Chem. Rev.* **88**, 1475–1498.
McCoy, A. J., Grosse-Kunstleve, R. W., Adams, P. D., Winn, M. D., Storoni, L. C. & Read, R. J. (2007). *J. Appl. Cryst.* **40**, 658–674.
McCoy, A. J., Grosse-Kunstleve, R. W., Storoni, L. C. & Read, R. J. (2005). *Acta Cryst.* D**61**, 458–464.
McPherson, A. (1982). *The Preparation and Analysis of Protein Crystals.* New York: John Wiley & Sons.
McPherson, A. (1987). *Crystallogr. Rev.* **1**, 191–250.
McPherson, A. (1992). *J. Cryst. Growth*, **122**, 161–167.
McPherson, A. (1996). *Crystallogr. Rev.* **6**, 157–305.
McPherson, A. (1997). *Trends Biotechnol.* **15**, 197–200.
McPherson, A. (1999). *Crystallization of Biological Macromolecules.* Cold Spring Harbor Laboratory Press.
McPherson, A. (2005). *Bioessays*, **27**, 447–458.
McPherson, A. (2013). *RNA Structure and Folding: Biophysical Techniques and Prediction Methods*, edited by K. Dagmar & H. Christian, pp. 125–156. Berlin, Boston: De Gruyter.
Matthews, B. W. (1968). *J. Mol. Biol.* **33**, 491–497.
Mirkov, T. E., Mathews, D. M., Du Plessis, D. H. & Dodds, J. A. (1989). *Virology*, **170**, 139–146.
Murshudov, G. N., Skubák, P., Lebedev, A. A., Pannu, N. S., Steiner, R. A., Nicholls, R. A., Winn, M. D., Long, F. & Vagin, A. A. (2011). *Acta Cryst.* D**67**, 355–367.
Natarajan, P., Lander, G. C., Shepherd, C. M., Reddy, V. S., Brooks, C. L. III & Johnson, J. E. (2005). *Nat. Rev.* **3**, 809–817.
Padilla, J. E. & Yeates, T. O. (2003). *Acta Cryst.* D**59**, 1124–1130.
Pflugrath, J. W. (1999). *Acta Cryst.* D**55**, 1718–1725.
Read, R. J. (2001). *Acta Cryst.* D**57**, 1373–1382.
Sims, J. L., Bush, L. P. & Atkinson, W. O. (1970). *J. Agric. Food Chem.* **18**, 381–384.
Stephanidis, B., Adichtchev, S., Gouet, P., McPherson, A. & Mermet, A. (2007). *Biophys. J.* **93**, 1354–1359.
Storoni, L. C., McCoy, A. J. & Read, R. J. (2004). *Acta Cryst.* D**60**, 432–438.
Valverde, R. A. & Dodds, J. A. (1986). *J. Gen. Virol.* **67**, 1875–1884.
Valverde, R. A. & Dodds, J. A. (1987). *J. Gen. Virol.* **68**, 965–972.
Valverde, R. A., Heick, J. A. & Dodds, J. A. (1991). *Phytopathology*, **81**, 99–104.
Winn, M. D., Ballard, C. C., Cowtan, K. D., Dodson, E. J., Emsley, P., Evans, P. R., Keegan, R. M., Krissinel, E. B., Leslie, A. G. W., McCoy, A., McNicholas, S. J., Murshudov, G. N., Pannu, N. S., Potterton, E. A., Powell, H. R., Read, R. J., Vagin, A. & Wilson, K. S. (2011). *Acta Cryst.* D**67**, 235–242.
Zeng, Y., Larson, S. B., Heitsch, C. E., McPherson, A. & Harvey, S. C. (2012). *J. Struct. Biol.* **180**, 110–116.